Influence of Reinforcement Characteristics and Ultrasonic-Assisted Stir-Casting Conditions on AA6061/Al_2O_3/SiC Tensile Strength: Machine Learning Modeling

[1]Rakesh S, [2]Malairaja R, [3]*Sriharini B

[1]Assistant Professor, Department of Mechanical Engineering, Francis Xavier Engineering College, Tirunelveli, Tamil Nadu, India.

[2]Assistant Professor, Department of Mechanical Engineering, Muthayammal Engineering College, Singlandhapuram, Tamil Nadu, India.

[3]*Department of Biomedical Engineering, Velalar College of Engineering and Technology (VCET), Erode, Tamil Nadu, India.

Email ID: [1]rrrrakesh56@gmail.com, [2]malairajamech16@gmail.com, [3]*sriharinib0520@gmail.com,

Abstract

The integration of machine learning (ML) with aluminium matrix composite manufacturing offers an effective approach for understanding the relationships between reinforcement characteristics, processing conditions, and mechanical performance. This study investigates the prediction of ultimate tensile strength (UTS) in AA6061 aluminium matrix nanocomposites containing Al_2O_3 and SiC nanoparticles using Gaussian Process Regression (GPR) and Least-Squares Boosting (LSBoost). A dataset comprising 240 observations was analysed using fourteen variables describing alloy composition, reinforcement concentration, particle dimensions, and ultrasonic-assisted stir-casting conditions. Eight reinforcement and processing variables were selected for predictive modelling, with 80% of the observations allocated to training and 20% to testing. Spearman correlation analysis identified SiC concentration (r_s = 0.66) and Al_2O_3 concentration (r_s = 0.47) as the variables most strongly associated with UTS. The predictive accuracy of both algorithms was assessed using the coefficient of determination (R^2), root mean square error (RMSE), and mean absolute error (MAE). GPR demonstrated superior predictive performance, achieving a testing R^2 of 0.9657, RMSE of approximately 2.85 MPa, and MAE of 2.28 MPa, compared with 0.9391, 3.80 MPa, and 3.12 MPa, respectively, for LSBoost. Residual analysis further indicated improved prediction consistency for GPR. LSBoost predictor-importance analysis highlighted the predominant influence of SiC and Al_2O_3 concentrations on the fitted tensile-strength response. These findings demonstrate the potential of GPR for modelling nonlinear composition–processing–property relationships and provide a computational foundation for further experimental investigation of ceramic-reinforced AA6061 composites.

Keywords: Mechanical Performance, Tensile strength, Residual analysis, Machine Learning, Least Square Boosting.

1. Introduction

The increasing complexity of experimental investigations has encouraged the adoption of data-driven approaches for predicting material behavior and optimizing processing conditions. Machine learning provides an effective framework for identifying hidden patterns, establishing relationships among experimental variables, and estimating performance characteristics with improved accuracy. Its application in materials science facilitates reliable property prediction, reduces extensive experimental trials, and supports the development of high-performance engineering materials. Quantum federated learning (QFL) was investigated using distributed quantum computing systems under heterogeneous channel conditions and

non-uniform data distributions. The proposed Joint EQFL integrated successive interference cancellation (SIC) and divergence-based clustering to improve convergence stability and learning efficiency (Chung et al., 2026). Reconfigurable intelligent surfaces (RISs) were employed in grant-free non-orthogonal multiple access (GF-NOMA) wireless networks to improve signal aggregation. The hybrid framework incorporated analog aggregation and SIC-based decoding, demonstrating improved convergence efficiency, aggregation accuracy, and robustness under heterogeneous data distributions (Atebawone et al., 2026). AA6061-T6 aluminium alloy coatings were deposited onto IS2062 steel through friction surfacing using engineered knurled surface patterns. FESEM revealed refined grains and defect-free interfaces, while EDX identified approximately 63 wt.% Al and 32 wt.% Fe. The R20 pattern achieved a maximum bonding strength of 15.4 kN and polarization resistance of 42.21 kΩ (Badheka et al., 2026).

AA6061 aluminium alloy and alumina–25 wt.% yttria-stabilized zirconia composites were joined through rotary friction welding at 630–2500 rpm. FESEM analysis revealed interfacial grain refinement, while dislocation density varied from 8.6×10^{15} to 12.7×10^{15} m^{-2}. Improved flexural strength and bonding integrity were observed at 630 rpm (Basheer Al-Naib, 2026). AA6061 aluminium composites reinforced with SiC, TiO_2, and fly ash at 3–12 wt.% were fabricated using stir casting. FESEM characterization supported microstructural evaluation, while tensile strength increased from 127 to 199 MPa and hardness from 55 to 86 HRB. The 9 wt.% reinforced composite exhibited a minimum wear rate of 0.00176 mm^3/m, as (Basavegowda et al., 2026). AA7075 and dissimilar AA5083/AA6061 aluminium alloy joints were investigated using friction stir welding and machine learning techniques. Auto-Encoder, LSTM, SVM, and GPR models were compared for tensile strength prediction, with the Auto-Encoder achieving an average prediction error of 5.679% for AA7075 (Luesak et al., 2026). Gaussian Process Regression (GPR) is an effective machine learning approach for predicting complex nonlinear relationships between processing variables and material properties, offering reliable predictions with uncertainty estimation. Field Emission Scanning Electron Microscopy (FESEM) provides detailed microstructural information on particle dispersion, interfacial adhesion, porosity (Prabakaran et al., 2026).

AA6061 aluminium alloy composites reinforced with plantain stem fibre ash, eucalyptus wood ash, and periwinkle shell particles at 0–15 wt.% were evaluated using Gaussian Process Regression. The Matérn GPR model achieved $R^2 = 0.992$, 0.994, and 0.994 for tensile strength, hardness, under replicate-holdout validation, although accuracy declined for unseen compositions (Barah et al., 2026). AA6061 aluminium metal matrix composites containing 0–15 vol.% Al_2O_3 particles were fabricated using friction extrusion. Hierarchical particle distribution promoted grain refinement and enhanced particle–matrix bonding, resulting in improved tensile strength while maintaining more than 20% ductility (Kalsar et al., 2026). AA6061-T6 aluminium alloy joints were fabricated using MIG welding at welding speeds of 40–70 mm/min and currents of 110–125 A. SEM fractography revealed ductile fracture with microvoid coalescence, while tensile strength ranged from 69 to 78 MPa, representing a 12–18% reduction compared with the base material (Machfuroh et al., 2026). AA6061 aluminium alloy reinforced with 4 wt.% SiC and 2–6 wt.% bamboo leaf ash-derived AlN was fabricated using stir casting. The optimum composite containing 4 wt.% AlN achieved a maximum tensile strength of 505 MPa, representing a 25.8% improvement over unreinforced AA6061 (Shanmugam et al., 2026).

AA7075/AA6061 aluminium alloys were joined through arc gas metal arc welding using ER4043 filler material. The welded joints achieved a elongation of 13.1%, maximum

tensile strength of 229.3 MPa and microhardness of 98 HV, while regression models exhibited $R^2 = 0.9787$ for tensile strength prediction (Bhadana et al., 2026). MIG-welded AA6061-T6 aluminium alloy joints exhibited a UTS of 69–78 MPa, with a 12–18% reduction compared with the base material. Welding speed significantly influenced joint strength, while heat-affected zone softening reduced mechanical performance (Machfuroh et al., 2026). Pitting corrosion in AA6061 aluminium alloy resulted in an 8–31% reduction in ultimate tensile strength (UTS) due to localized stress concentration and material degradation. Finite element modeling predicted UTS with errors generally within ±9%, while regression analysis supported residual strength prediction (AleAli et al., 2026). AA6061 aluminium hybrid composites reinforced with SiC and fly ash (FA) were fabricated through stir casting to improve mechanical properties. Grey Relational Analysis identified 9% SiC and 3% FA as the optimal composition for enhancing UTS, impact strength, and microhardness with a maximum GRG of 0.920 (Sahithi & Srilatha, 2026).

The mechanical performance of friction stir welded AA6061-T651 aluminium alloy was evaluated using Random Forest regression integrated with SHAP analysis. The predictive model achieved $R^2 \approx 0.84$ and RMSE ≈ 6 MPa for ultimate tensile strength, identifying rotational speed and axial load as dominant processing parameters (Uchegbulam et al., 2026). AA5083 and AA6061 aluminium alloys were joined using vortex friction stir welding to improve material mixing and microstructural refinement. The developed joints exhibited increased tensile strength from 123 to 182 MPa, microhardness from 97 to 112 HV, and elongation from 8.0% to 10.5% (Luo et al., 2027). Water-based nanofluids containing CuO, Ag, SiO_2, Cu, Al_2O_3, and TiO_2 nanoparticles were investigated for laminar boundary-layer flow over a moving flat plate. The least-squares homotopy perturbation method (LSHPM) exhibited lower absolute residual errors and faster convergence than HPM, with numerical validation performed using MATLAB bvp5c (Tahir et al., 2025).

The novelty of this study lies in integrating Gaussian Process Regression (GPR) and Least-Squares Boosting (LSBoost) with correlation analysis and predictor-importance assessment to investigate the tensile-strength behaviour of AA6061/Al_2O_3/SiC nanocomposites. Unlike approaches focusing primarily on reinforcement concentration, the developed framework incorporates alloy chemistry, nanoparticle characteristics, and ultrasonic-assisted stir-casting parameters within a unified modelling strategy. The comparative evaluation identifies GPR as the more accurate predictor ($R^2 = 0.9657$), while Spearman correlation and LSBoost feature importance highlight the dominant associations of SiC and Al_2O_3 concentrations with ultimate tensile strength. This integrated approach provides a basis for interpreting composition–processing–property relationships and guiding subsequent experimental investigations of hybrid ceramic-reinforced aluminium composites.

2. Materials and methods

2.1. Raw Materials and Composite Fabrication

AA6061 aluminium alloy was employed as the metallic matrix, while aluminium oxide (Al_2O_3) and silicon carbide (SiC) nanoparticles served as ceramic reinforcements. The elemental composition of the alloy was determined using X-ray fluorescence (XRF) spectroscopy, as presented in Table 1.

Table 1. Elemental composition of the AA6061 aluminium matrix.

Element	Si	Mg	Cu	Fe	Cr	Zn	Mn	Ti	Al

wt.%	0.64	0.93	0.24	0.31	0.16	0.08	0.07	0.04	Balance

The aluminium alloy was sectioned into smaller pieces and transferred to a graphite crucible positioned inside an electrically heated melting furnace. Temperature regulation was achieved using a K-type thermocouple, while mechanical agitation and ultrasonic processing were performed using a steel impeller and titanium sonotrode, respectively. The alloy was heated to 735 °C and maintained for 18 min to obtain a homogeneous molten phase. The ceramic powders were divided into smaller quantities, enclosed in aluminium foil, and heated to 425 °C before incorporation to facilitate particle wetting and dispersion.

The heated reinforcements were gradually introduced into the molten alloy under an argon atmosphere while mechanical agitation was maintained at 360 rpm for 12 min. Subsequently, ultrasonic dispers was applied through the immersed titanium sonotrode for 7 min to promote particle distribution and reduce agglomeration. The resulting melt was transferred into a cast-iron mould maintained at 375 °C, producing rectangular billets measuring 200 × 20 × 20 mm. The reinforcement proportions and specimen designations are provided in Table 2.

Table 2. Reinforcement concentrations and specimen identification.

Composition	Specimen code
AA6061 aluminium alloy	AS-0
AA6061 + 0.8 wt.% Al_2O_3	AS-1
AA6061 + 1.6 wt.% Al_2O_3	AS-2
AA6061 + 2.4 wt.% Al_2O_3	AS-3
AA6061 + 0.8 wt.% SiC	AS-4
AA6061 + 1.6 wt.% SiC	AS-5
AA6061 + 2.4 wt.% SiC	AS-6
AA6061 + 0.8 wt.% Al_2O_3 + 0.8 wt.% SiC	AS-7
AA6061 + 1.6 wt.% Al_2O_3 + 0.8 wt.% SiC	AS-8
AA6061 + 0.8 wt.% Al_2O_3 + 1.6 wt.% SiC	AS-9
AA6061 + 1.6 wt.% Al_2O_3 + 1.6 wt.% SiC	AS-10

2.2. Microstructural and Mechanical Evaluation

The surface morphology of the Al_2O_3 and SiC powders was examined through field-emission scanning electron microscopy (FESEM). Particle dimensions were evaluated using a nanoparticle tracking analyser following dispersion in ethanol and ultrasonic treatment for 8 min. Metallographic sections were prepared through sequential abrasion using SiC papers ranging from 240 to 2500 grit, followed by fine polishing with diamond suspension and colloidal silica. The polished surfaces were chemically etched using Keller's reagent containing 2 mL HF, 3 mL HNO_3, 5 mL HCl, and 190 mL deionized water. Optical microscopy was employed to examine grain morphology and solidification characteristics, whereas FESEM coupled with composition.

Tensile specimens were machined from the cast billets using wire electrical discharge machining in accordance with ASTM E8/E8M (Abushgair et al., 2026). Four specimens were considered for each composition to assess measurement repeatability. Mechanical testing was conducted at ambient temperature using a universal testing machine operating at a crosshead displacement rate of 0.8 mm/min. Ultimate tensile strength and percentage elongation were

determined from the recorded tensile responses. The relationship between material characteristics, manufacturing variables, and machine-learning-based tensile-strength estimation is illustrated in Fig. 1.

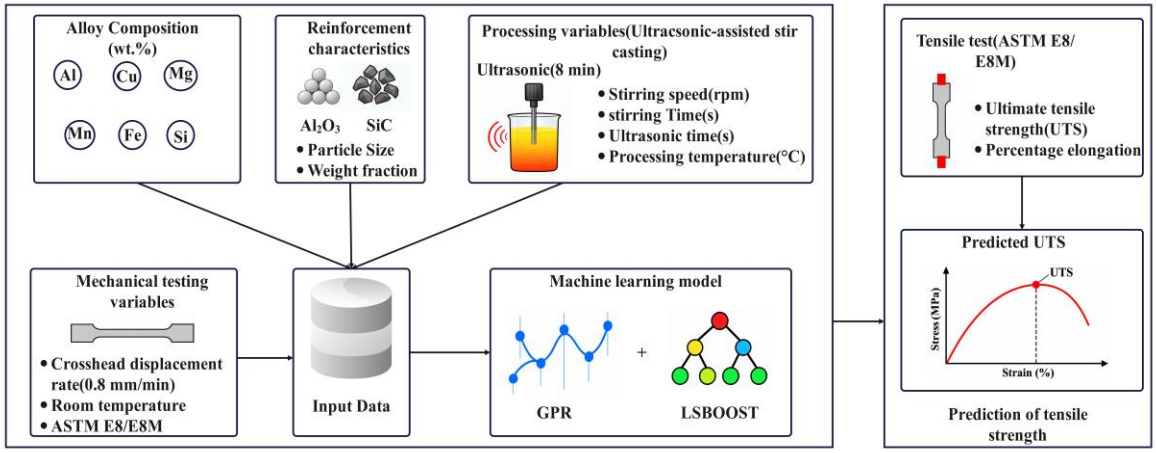

Figure. 1 Data-driven framework for tensile-strength prediction using alloy composition, reinforcement characteristics, processing variables, GPR, and LSBOOST regression.

2.3. Machine Learning Framework

2.3.1. Dataset Organization

The machine-learning framework was established to examine the relationship between alloy chemistry, reinforcement characteristics, manufacturing conditions, and ultimate tensile strength (UTS) of AA6061/Al_2O_3/SiC nanocomposites. The dataset contained 240 observations comprising fourteen input variables and two mechanical responses. Six variables represented the elemental composition of the aluminium matrix (Cu, Mn, Si, Mg, Zn, and Fe), while four described the reinforcement concentrations and particle sizes of Al_2O_3 and SiC. Casting temperature, stirring speed, stirring duration, and ultrasonication time constituted the remaining processing variables. UTS was considered the primary regression output, whereas elongation was included as an additional mechanical response. Table 3 presents the investigated parameter ranges.

Table 3. Input and output variables for tensile-property modelling.

Category	Parameter	Unit	Range
Alloy chemistry	Cu	wt.%	0.16–0.28
	Mn	wt.%	0.07–0.13
	Si	wt.%	0.54–0.70
	Mg	wt.%	0.84–1.04
	Zn	wt.%	0.08–0.16
	Fe	wt.%	0.24–0.36
Reinforcement	Al_2O_3 content	wt.%	0–2.4
	SiC content	wt.%	0–2.4
	Al_2O_3 particle size	nm	40–70
	SiC particle size	nm	60–90
Processing	Casting temperature	°C	715–755

	Stirring speed	rpm	300–420
	Stirring time	min	9–15
	Ultrasonication time	min	5–9
Mechanical response	UTS	MPa	
	Elongation	%	

2.3.2. Data Preparation and Visualization

The dataset was arranged into a numerical matrix to examine the distribution of material and manufacturing variables. Descriptive statistics and frequency histograms were used to evaluate the variations in elemental composition, reinforcement concentrations, particle dimensions, processing conditions, and mechanical responses. Correlation analysis was included to examine relationships among the investigated parameters.

To eliminate differences in numerical magnitude, the GPR input features were standardized using the mean and standard deviation of the training observations. The transformation was expressed as Eq. (1).

$$z_i = \frac{x_i - \mu}{\sigma} \tag{1}$$

The observations were divided into training and testing subsets at an 80:20 ratio, resulting in 192 training records and 48 testing records. Standardization parameters were obtained exclusively from the training subset to avoid information leakage.

2.3.3. Regression Model Development

Gaussian Process Regression (GPR) and Least-Squares Boosting (LSBoost) regression were used to establish the relationship between the input variables and UTS. GPR employs a probabilistic, covariance-based formulation to model nonlinear input-output behaviour. Its general expression is given in Eq. (2).

Gaussian Process Regression (GPR) $y(x) \sim \mathcal{GP}\big(m(x), k(x,x')\big)$ (2)

where $y(x)$ is the predicted response, $m(x)$ is the mean function, $k(x,x')$ is the covariance kernel function, and $\mathcal{GP}$ denotes a Gaussian process. Least-Squares Boosting (LSBoost) constructs an ensemble of weak regression trees in a sequential manner to minimize the prediction error. The model prediction can be written as Eq. (3).

Least-Squares Boosting (LSBoost)

$$\hat{y}(x) = \sum_{m=1}^{M} \nu h_m(x) \tag{3}$$

where $\hat{y}(x)$ is the predicted response, $h_m(x)$ is the mth regression tree, M is the total number of trees, and ν is the learning rate. The computational procedure for training, prediction, and performance evaluation of the two regression models is illustrated in Fig. 2.

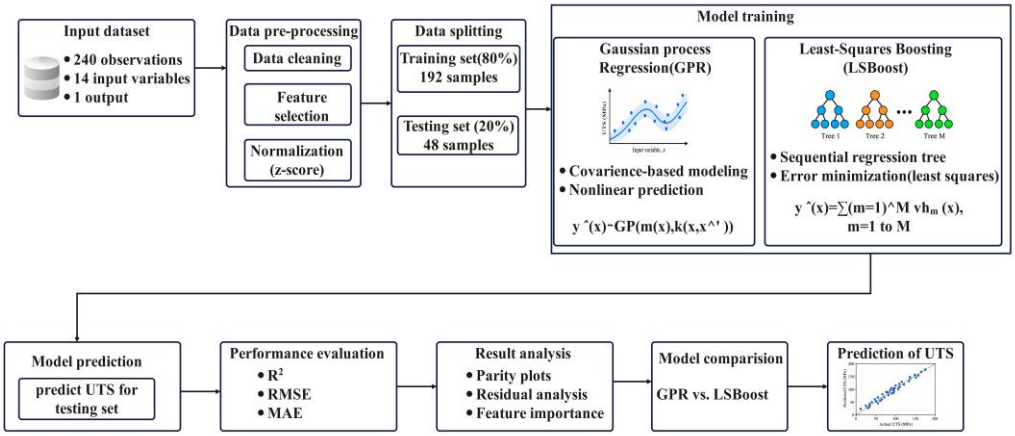

Fig. 2. Workflow of GPR and LSBoost training, prediction, and performance assessment.

2.3.4. Prediction Accuracy Assessment

The predictive capabilities of GPR and LSBOOST were evaluated using the coefficient of determination (R^2), root mean square error (RMSE), and mean absolute error (MAE). These indicators measure the explained response variation and differences between experimental and predicted tensile-strength values. Their mathematical formulations are presented in Eqs. (4)–(6).

Equation (4). Coefficient of determination

$$R^2 = 1 - \frac{\sum_{i=1}^{n} (y_i - \hat{y}_i)^2}{\sum_{i=1}^{n_i} (y_i - \bar{y})^2} \tag{4}$$

Equation (5). Root mean square error

$$RMSE = \sqrt{\frac{\sum_{i=1}^{n} (y_i - \hat{y}_i)^2}{n}} \tag{5}$$

Equation (6). Mean absolute error

$$MAE = \frac{1}{n}\sum_{i=1}^{n} |y_i - \hat{y}_i| \tag{6}$$

Higher R^2 values and lower RMSE and MAE values indicate improved prediction agreement.

2.3.5. Bayesian Hyperparameter Optimization

Bayesian optimization was selected as the hyperparameter search strategy for refining the regression models (Qu, 2026). The approach employs a probabilistic surrogate and acquisition function to explore promising parameter combinations while limiting unnecessary evaluations. For GPR, the search space can include covariance-kernel parameters, length scales, and noise regularization. For LSBOOST, the adjustable parameters include tree depth, learning rate, boosting iterations, and L2 regularization. The optimization objective is described by Eq. (7).

Equation (7). Bayesian optimization objective

$$\theta^* = \arg\min_{\theta} RMSE_{CV}(\theta) \quad (7)$$

Model selection and hyperparameter tuning should be performed using training observations, with the testing subset reserved for the final evaluation.

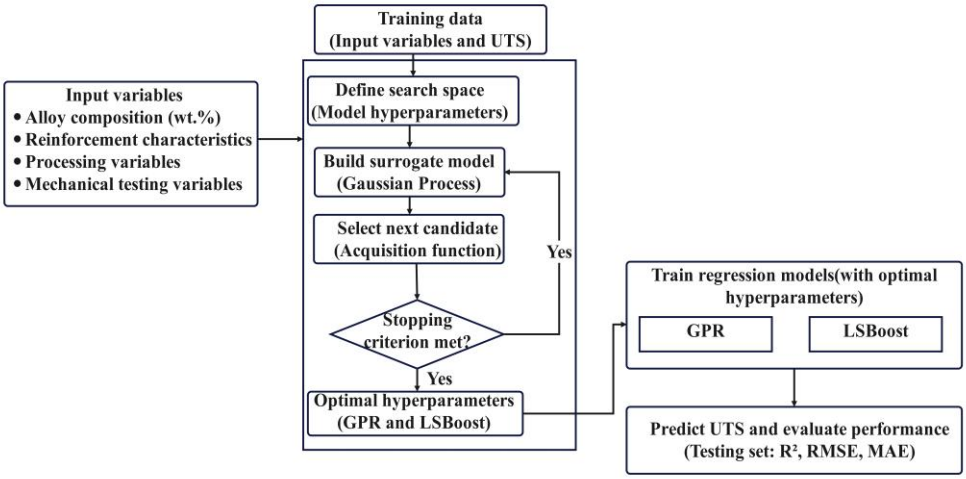

Fig. 3. Bayesian search procedure for regression hyperparameter tuning.

3. Results and discussion

In previous study, AA6061 aluminium alloy reinforced with SiC, B_4C, and TiC particles was fabricated through stir casting with reinforcement contents up to 2.1 wt.%. FESEM analysis revealed improved particle dispersion uniformity (PDI = 0.307–0.676) and grain refinement from 20.45 to 15.99 µm. The hybrid composite achieved a tensile strength of 254 MPa and hardness of 105 VHN, representing improvements of 68% and 118% (Kumar et al., 2026).

3.1. Reinforcement-Induced Microstructural Changes

Figure 4(a–c) presents the FESEM micrographs of the fractured surfaces of AA6061 aluminium alloy composites reinforced with Al_2O_3 and SiC nanoparticles at different magnifications. Figure 4(a) reveals a comparatively rough and heterogeneous fracture surface characterized by irregular surface ridges, localized cavities, and fractured regions. The presence of uneven surface features suggests nonuniform deformation and localized stress concentration during tensile loading. Several compact regions and irregularly distributed surface features are visible, indicating variations in the fracture morphology of the composite. The incorporation of ceramic reinforcements may influence crack propagation by restricting localized matrix deformation and modifying the fracture path. However, individual Al_2O_3 and SiC particles cannot be conclusively distinguished from the observed morphology alone.

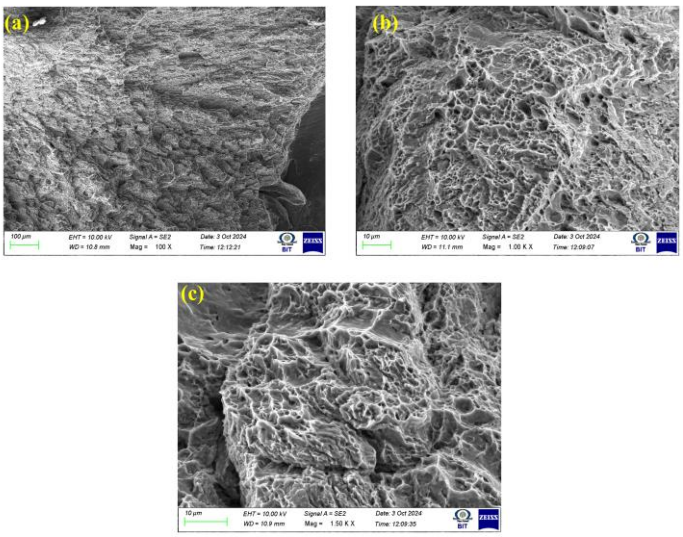

Figure. 4 FESEM microstructures AA6061/Al_2O_3/SiC composites.

Figure 4(b) exhibits a highly irregular fracture surface containing numerous interconnected cavities, fine dimples, and ligament-like structures. These features suggest considerable localized plastic deformation and microvoid formation during fracture. The presence of closely spaced cavities indicates that microvoid nucleation, growth, and coalescence may contribute to the failure mechanism. The surrounding stretched matrix regions suggest localized deformation before final separation. Reinforcement particles can influence this process by modifying stress distribution and restricting dislocation movement within the AA6061 matrix. The observed complex fracture morphology indicates that ductile fracture mechanisms may coexist with localized particle-associated damage.

Figure 4(c) provides a higher-magnification view of the fractured surface, revealing pronounced surface irregularities, interconnected microvoids, fractured ligaments, and localized tearing features. The comparatively deep cavities and rough fracture regions indicate substantial microvoid coalescence and localized matrix separation. The presence of irregularly shaped surface features suggests that cracks may propagate through multiple interconnected regions rather than along a uniform fracture plane. Such morphological characteristics are consistent with a predominantly ductile fracture process involving localized tearing, although reinforcement-related interfacial separation may also contribute. The ceramic nanoparticles could restrict plastic flow and alter local stress distributions, but direct evidence of particle pull-out or matrix–particle debonding requires additional elemental or high-resolution imaging.

The mechanical behavior of AA6061/Al_2O_3/SiC hybrid composites is influenced by reinforcement concentration, dispersion uniformity, interfacial bonding, and matrix deformation characteristics. Properly distributed ceramic nanoparticles can enhance the resistance to dislocation movement through Orowan strengthening, while grain refinement may contribute to strengthening through the Hall–Petch mechanism. Differences in thermal expansion between the aluminium matrix and ceramic reinforcements may also generate additional dislocations during cooling. Nevertheless, these strengthening mechanisms cannot be established directly from the presented fracture micrographs. The visible dimples, cavities, and fractured ligaments primarily provide evidence of localized plastic deformation and microvoid-related fracture processes.

Overall, the FESEM observations indicate that microvoid nucleation, growth, coalescence, and localized tearing are important fracture mechanisms in the examined AA6061/Al_2O_3/SiC composite. The rough fractured surfaces and interconnected cavities suggest a combination of plastic deformation and localized damage accumulation before failure. Although the ceramic reinforcements may improve tensile strength through particle strengthening and effective load transfer, excessive nanoparticle concentrations could encourage clustering, interfacial defects, and premature crack initiation. Therefore, the relationship between Al_2O_3/SiC reinforcement, fracture morphology, and ultimate tensile strength should be established through complementary mechanical testing, elemental mapping, and microstructural characterization.

Consequently, the influence of Al_2O_3 and SiC on ultimate tensile strength must be evaluated in relation to their concentration, particle dimensions, dispersion quality, and manufacturing conditions. The combined microstructural observations and tensile measurements are necessary to establish the relationship between reinforcement incorporation and mechanical performance. In previous work, AA6061 aluminium alloy reinforced with 2–3 wt.% SiC and 2 wt.% graphite nanoparticles was fabricated using stir-ultrasonic-squeeze casting. FESEM analysis revealed uniform nanoparticle dispersion and refined equiaxed grains analysis supported the presence of reinforcing constituents within the aluminium matrix. The optimum composite exhibited 28.48% higher hardness, 15.9% greater tensile strength, and 63.5% lower coefficient of friction (Pandey et al., 2026).

3.2. Machine Learning analysis

3.2.1. Data Distribution and Correlation

The statistical characteristics of the AA6061/Al_2O_3/SiC dataset were examined to identify variations in alloy chemistry, ceramic reinforcement, manufacturing conditions, and mechanical responses. Figure 5 presents the frequency distributions of the fourteen input parameters, ultimate tensile strength (UTS), and percentage elongation. The elemental concentrations exhibited variations within the investigated composition ranges, while the reinforcement concentrations, particle sizes, and processing parameters occurred at distinct operating levels. UTS values were distributed approximately between 143 and 210 MPa, with most observations concentrated around 160–190 MPa. The elongation values were predominantly distributed between 9 and 12.5%, indicating differences in the tensile response across the investigated material configurations. In earlier study, Full-duplex communication was investigated using a software-defined radio system operating at 2.4 GHz and 10 MHz bandwidth. Model-based self-interference cancellation achieved approximately 40 dB interference reduction under non-stationary data distributions with low computational complexity (Kim et al., 2024).

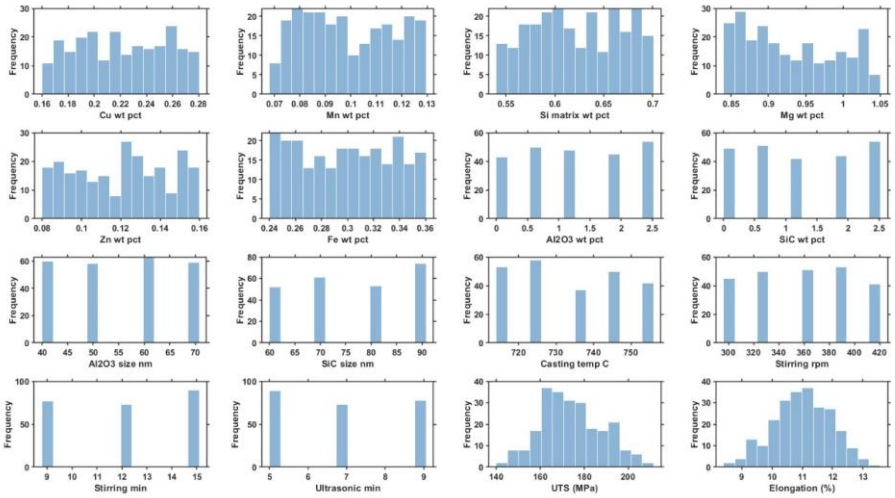

Fig. 5. Frequency distributions of material characteristics, processing variables, and mechanical responses.

Spearman rank correlation analysis was conducted to examine the relationships between the investigated parameters and UTS. The resulting correlation matrix is presented in Fig. 6. Among the reinforcement variables, SiC concentration exhibited the strongest positive association with UTS ($r_s = 0.66$), followed by Al_2O_3 concentration ($r_s = 0.47$). Stirring speed ($r_s = 0.19$), stirring duration ($r_s = 0.18$), and ultrasonication time ($r_s = 0.20$) showed weaker positive relationships. Conversely, Al_2O_3 and SiC particle sizes exhibited negative correlations of −0.12 and −0.10, respectively. The alloying elements displayed comparatively limited individual associations with UTS. Most correlations among the input parameters remained low, suggesting an absence of strong pairwise monotonic dependence. These findings indicate that reinforcement concentration was more closely associated with tensile-strength variation than the individual alloying and processing variables within the investigated dataset.

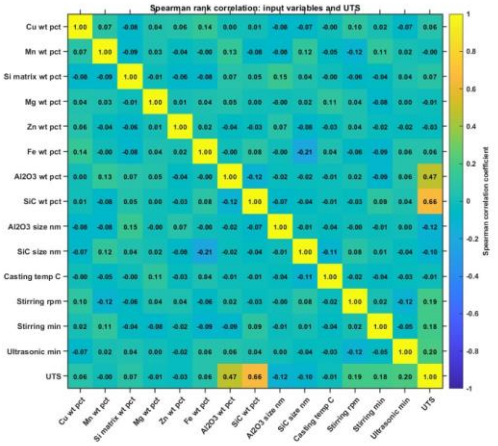

Fig. 6. Spearman correlation matrix of input variables and ultimate tensile strength.

3.2.2. Predictive Performance of GPR and LSBoost

The prediction capabilities of GPR and LSBoost were evaluated using an 80:20 data partition, comprising 192 training observations and 48 testing observations. Figure 7 compares the experimental UTS values with the corresponding model predictions. Both regression algorithms demonstrated close agreement with the experimental values, with most observations distributed near the ideal prediction line. GPR achieved a testing R^2 of 0.9657, whereas LSBoost produced an R^2 of 0.9391. The higher coefficient obtained by GPR indicates that it explained a greater proportion of the UTS variation within the testing subset.

The error metrics further supported this comparison. GPR achieved an RMSE of approximately 2.85 MPa and an MAE of 2.28 MPa, while LSBoost exhibited corresponding values of approximately 3.80 and 3.12 MPa. The lower prediction errors obtained by GPR indicate stronger agreement with the experimental values. Its covariance-based formulation effectively represented the continuous nonlinear relationships between reinforcement characteristics, processing variables, and UTS. LSBoost also demonstrated satisfactory predictive behaviour through the sequential combination of regression trees, although comparatively larger deviations were observed for several testing observations. In earlier work, SiO_2, $CaCO_3$, and Al_2O_3 nanoparticles were investigated for wettability alteration and enhanced condensate recovery in gas condensate reservoirs. Least Squares Boosting (LSBoost) was employed alongside other machine learning models, while SVM achieved superior accuracy for $CaCO_3$ with R^2 = 0.998, RMSE = 0.473, and MAPE = 0.491%. $CaCO_3$ nanoparticles enhanced condensate recovery by up to 18% (Akbari et al., 2026).

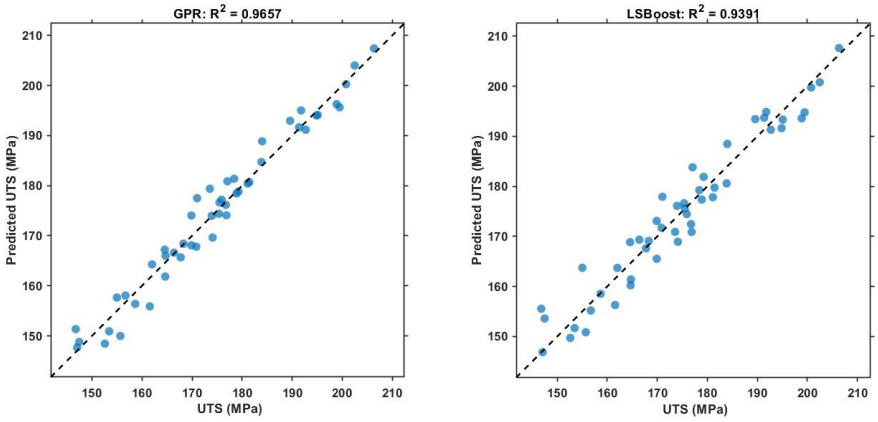

Fig. 7. Experimental versus predicted UTS for (a) GPR and (b) LSBoost.

3.2.3. Residual Error Assessment

Residual analysis was performed to examine the magnitude and distribution of prediction errors. Figure 8 presents the residual histograms and residual-versus-predicted UTS plots for both algorithms. The GPR residuals were concentrated around zero, with most deviations remaining within approximately ±5 MPa. A comparatively wider error distribution was observed for LSBoost, with negative residuals approaching −9 MPa and positive deviations reaching approximately 6 MPa.

The residual scatter plots showed no pronounced systematic variation across the investigated tensile-strength interval. Nevertheless, the LSBoost predictions exhibited greater dispersion than those of GPR, indicating reduced consistency for certain observations. The

relatively narrow residual distribution of GPR is consistent with its higher R^2 and lower error metrics. In previous investigation, fly ash-based geopolymer mortars incorporating SiO_2, Al_2O_3, and sand were compressive strength prediction using 280 experimental samples. Nonlinear Regression (NLR) achieved superior accuracy with $R^2 = 0.9483$ and RMSE = 5.14 MPa during training, while testing and validation yielded $R^2 = 0.937$ with minimal residual error dispersion (Malik et al., 2025).

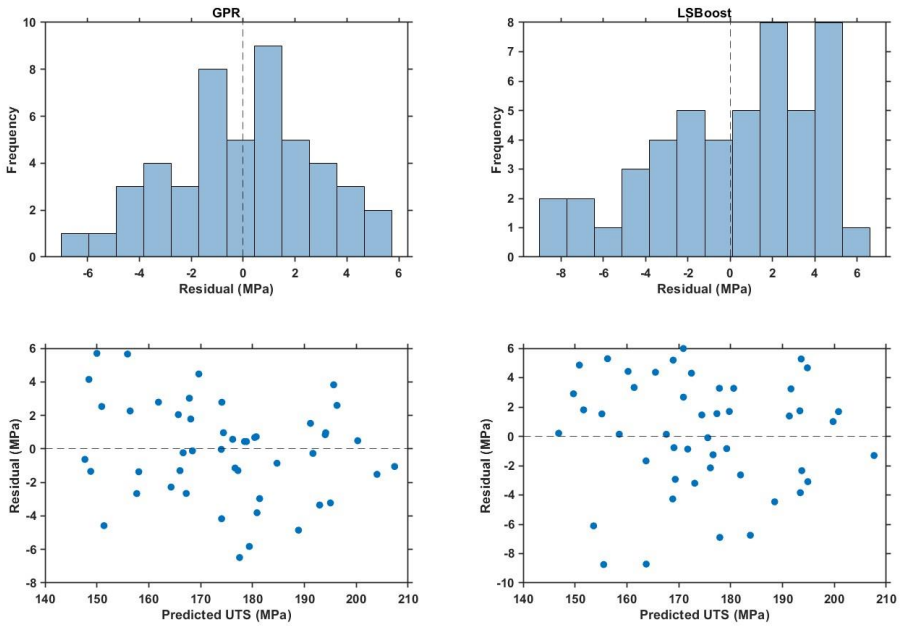

Fig. 8. Residual distributions and prediction-error patterns of (a, c) GPR and (b, d) LSBoost.

3.2.4. Comparative Model Evaluation

The statistical performances of the two regression models are compared in Fig. 9 and Table 5. GPR achieved the highest testing R^2 of 0.9657, compared with 0.9391 for LSBoost. Its RMSE and MAE were also lower, demonstrating improved predictive agreement. Although both algorithms achieved R^2 values exceeding 0.93, the overall results favoured GPR for UTS estimation within the evaluated dataset. In earlier work, AA6061-T6 aluminium alloy and AISI 304 stainless steel joints were investigated using friction stir spot welding (FSSW) through a coupled thermo-mechanical comparative model. The maximum simulated lap-shear strength metric was 5.85 kN, representing a 47.4% improvement, while the $R^2 = 0.9637$ and RMSE = 0.1688 kN (Mahmood, 2026).

Table 5. Comparative prediction accuracy of GPR and LSBoost.

Performance indicator	GPR	LSBoost
Testing R^2	0.9657	0.9391
RMSE (MPa)	≈ 2.85	≈ 3.80
MAE (MPa)	≈ 2.28	≈ 3.12
Testing observations	48	48

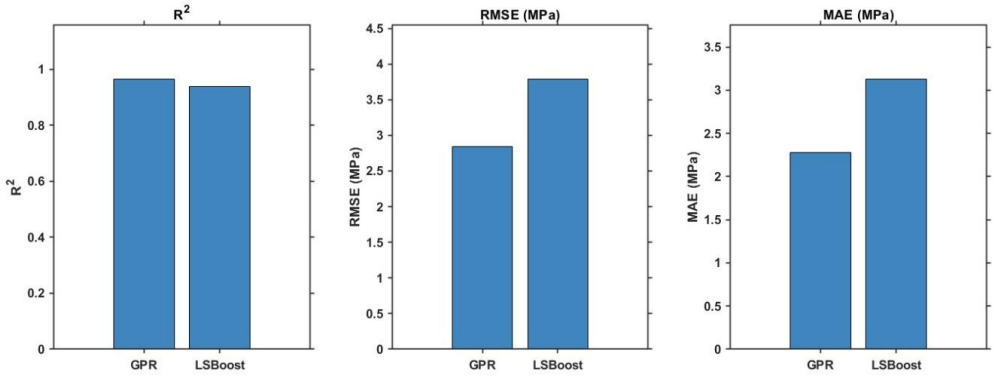

Fig. 9. Comparison of R^2, RMSE, and MAE for the regression models.

3.2.5. Predictor Importance and Tensile-Strength Trends

The contribution of individual input variables to LSBoost predictions was investigated through predictor-importance analysis, as illustrated in Fig. 10. SiC concentration exhibited the highest importance, followed by Al_2O_3 concentration. Stirring speed occupied the third position, whereas casting temperature, ultrasonication duration, and stirring time contributed comparatively smaller importance scores. Both nanoparticle-size variables exhibited relatively low importance.

The importance ranking was consistent with the correlation analysis, in which the two reinforcement concentrations demonstrated the strongest positive associations with UTS. The predominance of ceramic content suggests that the regression model relied principally on reinforcement concentration to distinguish tensile-strength variations. Nevertheless, predictor importance describes the contribution of each variable to the fitted model and should not be interpreted as a direct measure of its physical strengthening contribution.

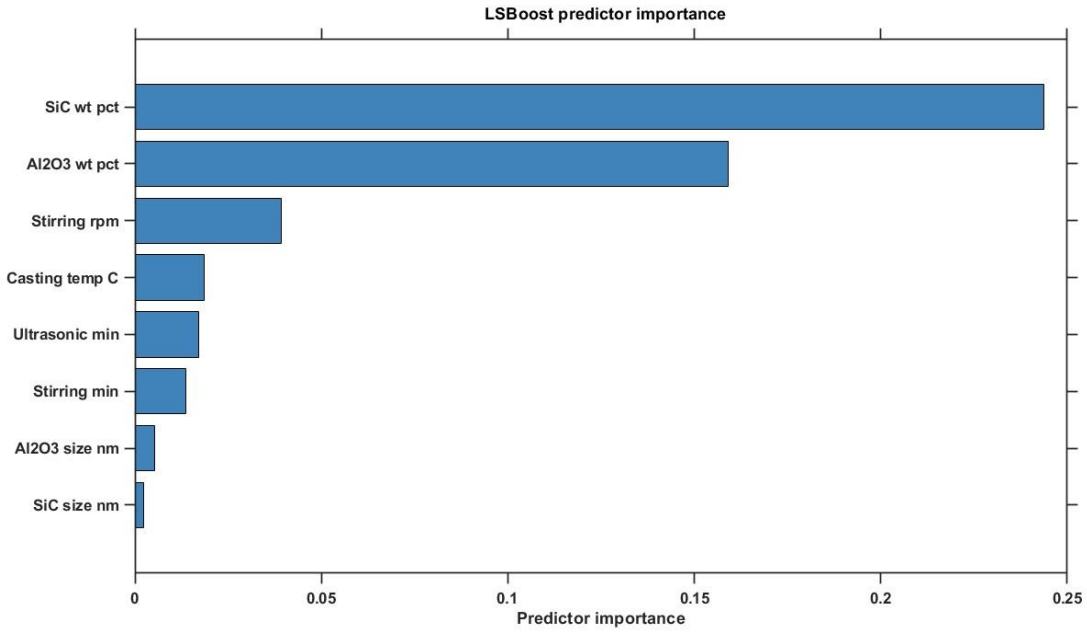

Fig. 10. LSBoost predictor-importance ranking for UTS estimation.

The relationships between the eight predictive variables and UTS are further illustrated in Fig. 11. Increasing Al_2O_3 and SiC concentrations was generally associated with higher tensile-strength values, although substantial variation occurred at individual reinforcement levels. Casting temperature and stirring speed displayed more dispersed relationships, while particle dimensions and processing durations showed comparatively weak individual trends.

These observations indicate that tensile-strength variation cannot be explained by a single manufacturing variable. Instead, the combined effects of reinforcement concentration, particle characteristics, and processing conditions must be considered when interpreting the predicted response. The nonlinear regression framework provides a means of examining these interactions within the investigated parameter ranges. In earlier research, AA6061 and AA7075 aluminium alloys were joined using friction stir welding (FSW) and tungsten inert gas (TIG) welding processes. FSW performed at 1000 rpm and 60 mm/min achieved a maximum tensile strength of 268 MPa, representing a 29% improvement over TIG welding, along with a maximum microhardness of 122 HV (Ramesh et al., 2026).

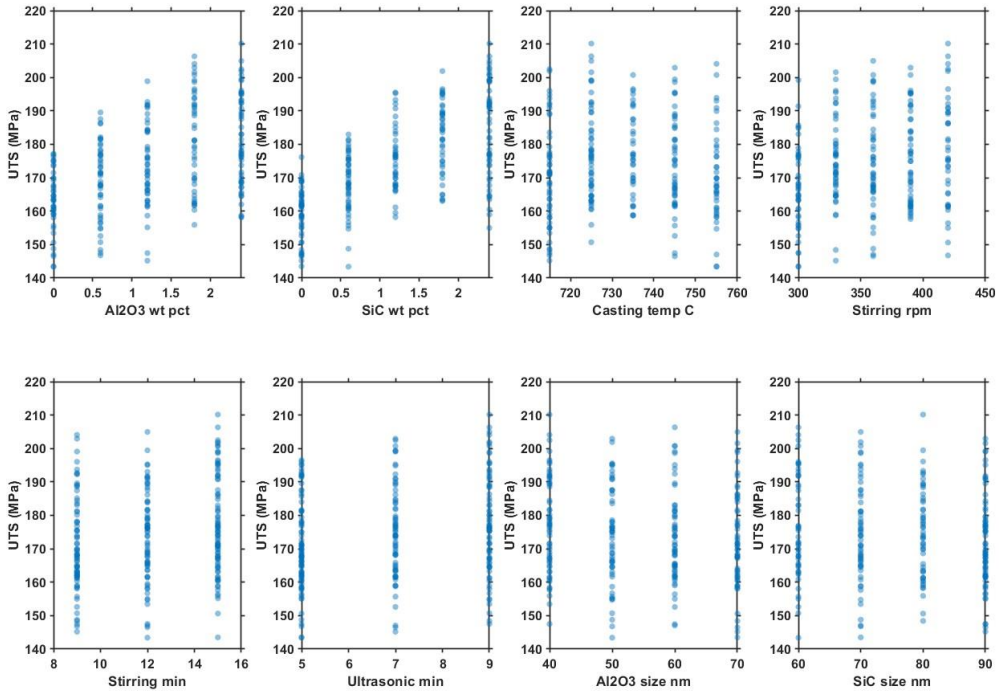

Fig. 11. Relationships between reinforcement, casting parameters, and UTS.

3.2.6. Prediction Agreement Across Testing Observations

Figure 12 compares the experimental UTS values with the corresponding GPR and LSBoost predictions for the 48 testing observations. Both models reproduced the principal variations in tensile strength, including the alternating high- and low-strength observations. The GPR prediction curve followed the experimental values more closely across most of the testing sequence, whereas LSBoost displayed larger deviations at selected observations.

The agreement between the experimental and predicted curves supports the comparative performance metrics and residual analysis. Overall, GPR demonstrated stronger predictive consistency than LSBoost for the investigated AA6061/Al_2O_3/SiC dataset, while

both approaches captured the principal relationships between reinforcement characteristics, processing conditions, and tensile strength. In previous study, AA6061/AA7075 aluminium alloys were investigated using friction stir additive manufacturing (FSAM) at rotational speeds of 1000–1200 rpm, traverse speeds of 30–40 mm/min, and tilt angles of 1.0–2.2°. Gaussian Process Regression (GPR) achieved $R^2 > 0.85$ and tensile strength prediction errors of 2.34–8.67 MPa using 882 synthetic samples derived from nine experimental observations (Venkatachalam et al., 2026).

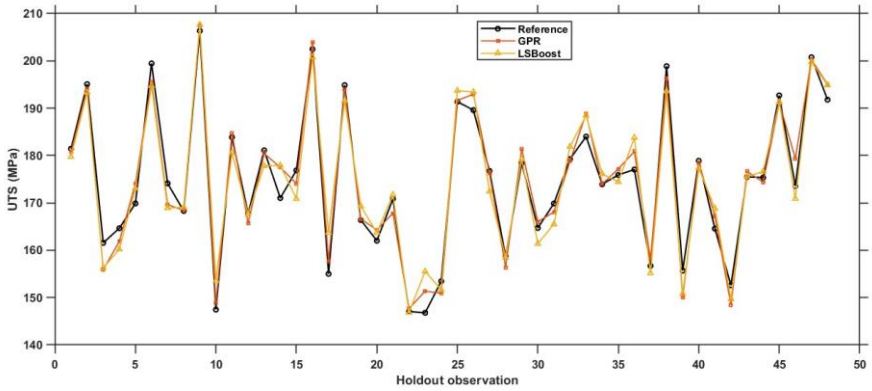

Fig. 12. Comparison of experimental and predicted UTS across the testing observations.

4. Conclusion

The present investigation examined the application of Gaussian Process Regression (GPR) and Least-Squares Boosting (LSBoost) for predicting the ultimate tensile strength (UTS) of AA6061 aluminium composites reinforced with Al_2O_3 and SiC nanoparticles. The modelling framework considered alloy chemistry, ceramic reinforcement characteristics, and ultrasonic-assisted stir-casting parameters to evaluate their relationships with tensile behaviour. The principal findings are summarized below.

- The microstructural evaluation framework considered nanoparticle dispersion, grain morphology, and reinforcement–matrix interactions. FESEM, and optical microscopy are necessary to establish the extent of particle distribution, grain refinement, and casting porosity in the fabricated composites.

- Spearman correlation analysis identified SiC and Al_2O_3 concentrations as the variables most strongly associated with UTS, with correlation coefficients of 0.66 and 0.47, respectively. Stirring speed, stirring duration, and ultrasonication time exhibited weaker positive correlations of 0.19, 0.18, and 0.20.

- Both regression models demonstrated strong agreement with the experimental UTS values. GPR achieved a testing R^2 of **0.9657**, outperforming LSBoost, which recorded **0.9391**. The corresponding RMSE values were approximately 2.85 and 3.80 MPa, respectively.

- Residual analysis indicated that GPR produced a narrower error distribution and more consistent predictions than LSBoost. The experimental -versus-predicted plots further demonstrated the ability of both algorithms to represent variations in tensile strength across the investigated observations.

- LSBoost predictor-importance analysis identified SiC concentration as the most influential variable, followed by Al_2O_3 content and stirring speed. Particle sizes contributed comparatively less to the fitted model, indicating that reinforcement concentration played a greater role in its predictions.

- The combined correlation, prediction, and feature-importance analyses demonstrated the usefulness of GPR and LSBoost for examining nonlinear relationships between material characteristics, manufacturing parameters, and tensile-strength responses.

Overall, GPR exhibited superior predictive performance for the evaluated dataset. The findings provide a computational basis for further investigation of AA6061/Al_2O_3/SiC nanocomposites, while independent experimental validation is required to establish predictive reliability under actual manufacturing conditions.

References

Abushgair, K., Haddad, M., Alzubi, E., Atieh, A., & Alshoul, M. (2026). Restoring welded inconel 625 integrity: a comprehensive multi-technique analysis of optimized post-weld heat treatment. *Journal of Materials Science: Materials in Engineering*, *21*(1). https://doi.org/10.1186/s40712-025-00384-8

Akbari, A., Seifi, F., Kazemzadeh, Y., & Ahmadi, S. (2026). Machine learning and nanoparticles for enhancing condensate recovery in gas condensate reservoirs. *Canadian Journal of Chemical Engineering*, *104*(4), 1959–1989. https://doi.org/10.1002/cjce.70119

AleAli, R., Karimi, H. R., Danaee, I., & Jabbar, M. A. (2026). Morphology-based mechanical degradation model for failure behavior of surface-pitted 6061 aluminum using experimental and finite element analysis. *Results in Engineering*, *32*. https://doi.org/10.1016/j.rineng.2026.112929

Atebawone, E., Obour Agyekum, K. O.-B., Dzisi Gadze, J., Opare, K. A.-B., Antwi, O. A., & Akromond, R. (2026). A RIS-Programmable hybrid uplink for grant-Free NOMA networks with distributed signal aggregation. *Physical Communication*, *75*. https://doi.org/10.1016/j.phycom.2026.103047

Badheka, K., Sharma, D. K., & Badheka, V. (2026). Role of knurled surface topography of IS2062 steel in influencing the mechanical integrity and microstructural evolution of friction-surfaced AA6061 coatings. *Surface Engineering*. https://doi.org/10.1177/02670844261461410

Barah, O. O., Otaru, A. J., Bori, I., & Khalil, S. F. (2026). Composition-holdout validation of gaussian-process surrogates for reliability-aware multi-property prediction in AA6061 hybrid composites. *International Journal of Material Forming*, *19*(3). https://doi.org/10.1007/s12289-026-02081-z

Basavegowda, N., Azeem Hafiz, P. A., Tonk, A., Paramasivam, K., Kailasam, C., Kesavan, A., Saminathan, K., Sivasamy, N., & Mishra, P. (2026). Development and Tribological Evaluation of Stir-Cast AA6061/SiC-TiO2-Fly Ash Hybrid Composites for High-Performance Automotive Components. *Tribology Transactions*. https://doi.org/10.1080/10402004.2026.2688193

Basheer Al-Naib, U. M. (2026). Dislocation Mechanics and Interfacial Grain Refinement in Dissimilar Metal–Ceramic Friction Welds: A Case Study on AA6061/Alumina-25 wt.% YSZ. *Journal of Materials Engineering and Performance*, *35*(17), 17060–17072. https://doi.org/10.1007/s11665-025-12824-9

Bhadana, M., Bhardwaj, P., Mehdi, H., & Mouria, P. K. (2026). Parametric optimization of RA-GMAW welded joints of dissimilar AA6061/AA7075 welded joints using filler ER4043. *International Journal on Interactive Design and Manufacturing*, *20*(5), 2555–2574. https://doi.org/10.1007/s12008-026-02510-y

Chung, J., Im, C., Park, S., Kim, J., & Lee, W. (2026). Quantum Federated Gradient Aggregation Using the Parameter-Shift Rule. *IEEE Internet of Things Journal*, *13*(11), 25367–25379. https://doi.org/10.1109/JIOT.2026.3677003

Kalsar, R., Schuessler, B. J., Li, L., Wang, T., Darsell, J. T., Ma, X., Soulami, A., Herling, D. R., Lavender, C. A., & Joshi, V. V. (2026). Achieving strength-ductility synergy in hierarchical aluminum metal matrix composites via friction extrusion. *Communications Materials*, *7*(1). https://doi.org/10.1038/s43246-025-01049-x

Kim, J., Lee, H., Do, H., Choi, J., Park, J., Shin, W., Eldar, Y. C., & Lee, N. (2024). On the Learning of Digital Self-Interference Cancellation in Full-Duplex Radios. *IEEE Wireless Communications*, *31*(4), 184–191. https://doi.org/10.1109/MWC.014.2300403

Kumar, S., Agrawal, G. K., Chawla, B. S., & Kumar, R. (2026). Influence of hybrid ceramic reinforcements (SiC, B4C, TiC) on the microstructural stability and tensile behavior of stir-cast Al6061 composites. *Engineering Research Express*, *8*(17). https://doi.org/10.1088/2631-8695/ae966c

Luesak, P., Sirirak, W., Matitopanum, S., Srichok, T., Khonjun, S., Chiaranai, S., Jirasirilerd, G., & Gonwirat, S. (2026). Machine learning-based prediction of friction stir welding parameters for optimized tensile strength in aluminum alloys. *International Journal on Interactive Design and Manufacturing*, *20*(4), 1963–1995. https://doi.org/10.1007/s12008-025-02433-0

Luo, J., Satish Kumar, T., Alamri, S., & Liu, S. (2027). Novel study of joining of AA6061 and AA5083 sheets by using vortex friction stir welding. *Vacuum*, *255*. https://doi.org/10.1016/j.vacuum.2026.115808

Machfuroh, T., Witono, K., Agustriyana, L., Rosady, S. D. N., Puspitasari, E., & Emzain, Z. F. (2026). Mechanical performance and haz softening behavior of mig-welded AA6061 aluminium under varying welding parameters. *Journal of Engineering and Applied Science*, *73*(1). https://doi.org/10.1186/s44147-026-00939-2

Mahmood, Y. S. (2026). Thermo-Mechanical Optimization of Tool Geometry Ratios in Dissimilar AA6061-T6 Aluminum/AISI 304 Stainless Steel Friction Stir Spot Welding: A Fully Coupled Multiphysics Approach. *Annales de Chimie: Science Des Materiaux*, *50*(4), 395–407. https://doi.org/10.18280/acsm.500408

Malik, S., Arunachalam, K. P., Algburi, S., Oza, A. D., Mohammed, S. J., Al-Baghdadi, A. H., Majdi, H. S., & Tufail, M. S. (2025). Statistical and machine learning models for

predicting the compressive strength of fly ash-based geopolymer mortar. *Asian Journal of Civil Engineering*, *26*(10), 4251–4268. https://doi.org/10.1007/s42107-025-01423-7

Pandey, U., Ghose, J., Acherjee, B., & Paul, G. (2026). Mechanical and Tribological Performance of AA6061 Hybrid Nanocomposites Produced by Stir-Ultrasonic-Squeeze Casting Method. *Journal of Materials Engineering and Performance*, *35*(8), 7259–7273. https://doi.org/10.1007/s11665-025-12169-3

Prabakaran, V., Venkatasudhahar, M., Jayabal, R., Rayappan, M. N. F., Kumaravel, A. S., & Murugan, K. (2026). Study of tribological and corrosion behavior of AA6061–SiC–WS_2/WSe_2 hybrid composites using the taguchi method. *Journal of Engineering and Applied Science*, *73*(1). https://doi.org/10.1186/s44147-026-00977-w

Qu, X. (2026). Multi-Modal Data Fusion And Graph Neural Network For Real-Time Anomaly Diagnosis In CNC Turning Processes. *Journal of Applied Science and Engineering*, *31*. https://doi.org/10.6180/jase.202608_31.032

Ramesh, M., Suresh, T., Dhanesh, G., Prasanth, D. D., Irfan, M. M., & Sampath, H. V. (2026). A comparative study on friction stir and TIG welding of dissimilar AA6061–AA7075 aluminium alloys. *Interactions*, *247*(1). https://doi.org/10.1007/s10751-026-02411-2

Sahithi, V. V. D., & Srilatha, N. (2026). Multi-objective optimization of aluminum hybrid composites using grey relational analysis. *Interactions*, *247*(1). https://doi.org/10.1007/s10751-026-02715-3

Shanmugam, S. K., Kumar, A., Singh, N., Patel, M. C., Prasad, P. R., & Thanikasalam, A. (2026). High-performance sustainable AA6061–SiC–AlN hybrid composites reinforced with bamboo-derived AlN. *Interactions*, *247*(1). https://doi.org/10.1007/s10751-026-02564-0

Tahir, M., Rafiq, M., Aidara, C. A. T., & Bashir, Y. (2025). Analytical and numerical investigation of various nanofluid boundary layer flow across a moving flat plate. *AIP Advances*, *15*(8). https://doi.org/10.1063/5.0284173

Uchegbulam, I., Opuwill, S. C., Nnoka, M., & Jack, T. A. (2026). Machine learning modelling of friction stir welded AA6061-T651 tensile strength using random forest and SHAP analysis. *International Journal of Advanced Manufacturing Technology*, *145*(3–4), 2615–2628. https://doi.org/10.1007/s00170-026-18430-w

Venkatachalam, K., Selvaraj, S. K., Mannayee, G., Pattabiraman, K., & Sundaramali, G. (2026). RBF-assisted surrogate modeling and machine learning for mechanical property prediction in friction stir additive manufacturing: Application to dissimilar AA6061/AA7075 aluminum alloys. *Scientific Reports*, *16*(1). https://doi.org/10.1038/s41598-026-42608-7